

Neural Architecture Search based Global-local Vision Mamba for Palm-Vein Recognition

Huafeng Qin, Yuming Fu, Jing Chen, Mounim A. El-Yacoubi, Xinbo Gao, *Fellow, IEEE* and Jun Wang

Abstract—Due to the advantages such as high security, high privacy, and liveness recognition, vein recognition has been received more and more attention in past years. Recently, deep learning models, *e.g.*, Mamba has shown robust feature representation with linear computational complexity and successfully applied for visual tasks. However, vision Mamba can capture long-distance feature dependencies but unfortunately deteriorate local feature details. Besides, manually designing a Mamba architecture based on human priori knowledge is very time-consuming and error-prone. In this paper, first, we propose a hybrid network structure named Global-local Vision Mamba (GLVM), to learn the local correlations in images explicitly and global dependencies among tokens for vein feature representation. Secondly, we design a Multi-head Mamba to learn the dependencies along different directions, so as to improve the feature representation ability of vision Mamba. Thirdly, to learn the complementary features, we propose a ConvMamba block consisting of three branches, named Multi-head Mamba branch (MHMamba), Feature Iteration Unit branch (FIU), and Convolutional Neural Network (CNN) branch, where the Feature Iteration Unit branch aims to fuse convolutional local features with Mamba-based global representations. Finally, a Global-local Alternate Neural Architecture Search (GLNAS) method is proposed to search the optimal architecture of GLVM alternately with the evolutionary algorithm, thereby improving the recognition performance for vein recognition tasks. We conduct rigorous experiments on three public palm-vein databases to estimate the performance. The experimental results demonstrate that the proposed method outperforms the representative approaches and achieves state-of-the-art recognition accuracy.

Index Terms—Palm-vein recognition, Mamba, Neural architecture search (NAS), Deep-learning.

I. INTRODUCTION

As a powerful tool for information security, biometric technology has received increasing attention. Biometric technology accurately recognizes individual identity by analyzing individual physiological or behavioral characteristics, such as face [1], fingerprints [2], iris [3], eye movement [4], *etc.* However, with the popular applications, traditional recognition methods have gradually shown their shortcomings in security

H. Qin and Y. Fu are with the School of Computer Science and Information Engineering, Chongqing Technology and Business University, Chongqing 400067, China (e-mail: qinhuafengfeng@163.com, fym291715@163.com).

M. A. El-Yacoubi is with SAMOVAR, Telecom SudParis, Institut Polytechnique de Paris, 91120 Palaiseau, France (e-mail: mounim.el_yacoubi@telecom-sudparis.eu).

X. Gao is with the Chongqing Key Laboratory of Image Cognition, Chongqing University of Posts and Telecommunications, Chongqing 400065, China (e-mail: gaoxb@cqupt.edu.cn).

J. Wang is with the College of Computer Science, China University of Mining and Technology, Jiangsu 221116, China (e-mail: WJ999LX@163.com).

Manuscript received September XX, 2023; revised XXXX XX, 201X. (Corresponding author: Xinbo Gao.)

Manuscript received April 19, 2021; revised August 16, 2021.

and convenience. Compared with traditional biometric methods, vein recognition technology has attracted more attention due to its advantages of high security and privacy [5]. Vein recognition technology utilizes the nature of the deoxygenated hemoglobin in the blood to absorb near-infrared light for image collection. Specifically, when near-infrared light with a wavelength of 700nm-1000nm passes through our body, the hemoglobin absorbs near-infrared light. Therefore, the camera can capture vein patterns because the vein vessels in the image are darker than the surrounding area, resulting in unique vein feature information of the individual. The vein recognition technology has drawn increasing attention in recent years.

A. Motivation

Currently, various approaches have been investigated for the vein recognition task. For example, the researchers design handcrafted descriptors, *i.e.*, maximum Curvature [6], repeated line tracking [7], LLBP [8], and compact multi-representation feature descriptor [9] to extract the vein feature. However, such approaches are highly dependent on the designer's professional experience and prior knowledge and their representation capacity is limited, resulting in poor performance.

Recently, deep learning neural networks have shown robust feature representation capacity and achieved promising performance in various tasks such as image classification [10, 11] and data augmentation [12, 13]. Inspired by its successful application, some researchers brought it into vein recognition. In recent years, various deep learning approaches [14, 15, 16, 17, 18] have been proposed for vein recognition, and shows super performance compared to traditional vein recognition approaches, *i.e.* handcrafted approaches [6, 7, 8] and traditional machine learning approaches [19, 20, 21, 22, 23].

These deep learning-based vein recognition approaches are mainly divided into two categories: CNN-based vein recognition approaches [15, 17, 24, 25] and Transformer-based vein recognition approaches [26, 27]. Due to the parameters sharing and local perception, the CNN [10, 17] shows natural advantages for image-based vision tasks, *e.g.*, the 2D structure, and spatial local information. Therefore, the CNN-based vein recognition approaches achieve significant improvement in terms of recognition accuracy. However, they are struggling to pay less attention to global dependencies due to the limited local receptive field [28], which are as important as local dependencies. Transformer [29] first proposed for Natural Language Processing (NLP) has been successfully introduced into the field of computer vision by Vision Transformer (ViT) [11] and shows excellent performance. Thanks to the

attention mechanism, the Transformers are capable of capturing long-term dependencies between different positions in an input sequence and have shown excellent performance for vein recognition. Nevertheless, the self-attention mechanism in Transformers results in low inference speed and huge memory usage when processing long-sequence visual tasks [30]. Recently, the state space models (SSMs)[31] have shown great potential for long sequence modeling with linear complexity. These models can be seen as a combination of Recurrent Neural Networks (RNNs) and Convolutional Neural Networks (CNNs). Some researchers incorporate time-varying parameters into the SSM and propose a hardware-aware algorithm named Mamba [32] for more efficient training and inference. Inspired by the success of Mamba [32], a novel variant has been investigated for vision tasks such as image classification [30, 33, 34], image segmentation [35, 36] and synthesis [37], and achieve comparable or superior performance compared to CNNs and ViT [11]. The superior scaling performance of Mamba implies that it contributes as an alternative foundation model to Transformer [30]. Unfortunately, there are some limits to deep learning-based models on vein recognition tasks:

- The Mamba has been successfully applied for processing visual data such as natural images and videos, but a generic pure-SSM-based backbone network has not been explored for biometric, *e.g.* vein recognition. Besides, as described in aforementioned works [30, 31], the SSMs exhibit linear or near-linear computational complexity with sequence length and have principled mechanisms for modeling long-term dependencies, making them particularly suited for handling long-sequence data. However, similar to Vision Transformer, Mamba may ignore the local relation and the structure information inside the patch, which are as important as global dependencies [38], so it is worth exploring a mechanism to take both compensation features for enhanced representation learning of Mamba.
- Existing works mainly adopt the deep learning network architecture manually designed by human experts for vein recognition, which suffers from the following drawbacks. First, it is very time-consuming to design such an architecture manually as there are too many factors to consider. Second, there are a huge candidate network architecture space, so experts may not be able to explore the entire design space of DNN architectures, resulting in finding the sub-optimal hyperparameters. Thirdly, it is difficult to directly employ manually designed architectures to other datasets or more complex tasks, limiting their application in the real world. To address this problem, Neural Architecture Search (NAS) [39, 40, 41, 42] technology shows great potential in automatically searching network architecture. Jia et.al [43] introduced the NAS for 2D and 3D palmprint recognition and palm vein recognition. Subsequently, an Attention Gated recurrent unit-based Neural Architecture Search (AGNAS) [44] is proposed to automatically find the optimal network architecture for finger-vein recognition tasks. The main-stream fast Neural Architecture Search methods [42, 44, 45] samples candidate sub-network from the supernet during each training iteration and the

optimal sub-network is determined for training and testing. However, they can not work well on the huge search space because there is a low correlation between the retrained subnet and the subnet sampled from the supernet.

B. Our work

To address these limits, in this paper, we propose a Global-local Vision Mamba (GLVM) to capture local and global features for vein recognition. The proposed GLVM is stacked by multiple ConvMamba modules, each of which comprises three crucial modules: CNN branch, Multi-head Mamba (MHMamba) branch, and Feature Interaction Unit branch. The CNN branch is responsible for extracting the local details while the MHMamba branch aims to capture the global dependencies representation, the Feature Interaction Unit branch combines convolutional local features with MHMamba-based global representations in a complementary. Therefore, the proposed GLVM is capable of learning robust features for vein recognition. To automatically search the architecture of our GLVM, we design a novel Global-local Neural Network Search (GLANAS) strategy to find the optimal networks. Specifically, the huge search space for GLANAS is split into two sub-spaces: global search space and local search space. We alternately search global hyperparameters and local hyperparameters with an evolutionary algorithm to obtain optimal architecture. Compared with traditional search strategies, the proposed GLANAS can stabilize the search process and improve the search performance.

To summarize, the main contributions are as follows:

- To our best knowledge, this work makes the first attempt to accommodate Mamba model on the vein recognition task and investigates a Global-local vision Mamba (GLVM) to enhance the vein feature learning capacity.
- We propose a Multi-head Mamba (MHMamba) module with a multi-direction scanning mechanism to improve the feature representation capacity. Besides, the GLVM is developed by integrating the CNN branch, MHMamba branch and Feature Interaction Unit branch to learn local features and global representations for vein recognition.
- We are the first to explore better Mamba architecture by NAS for vein recognition. We design a Global-local Alternating Neural Network Search algorithm (GLANAS) to find the optimal architecture hyperparameters of the proposed GLVM for vein recognition.
- We conduct rigorous experiments on three public palm-vein databases to evaluate the performance of the proposed methods. The experimental results show that our methods achieve the highest performance among all comparable methods.

II. RELATED WORKS

A. Traditional Vein Recognition Algorithms

Traditional vein recognition algorithms can be divided into two categories: (1) Handcrafted algorithms. The handcrafted algorithms rely on manually designed descriptors to extract vein texture features, such as curvature-based methods [6, 46], local binary pattern-based methods [47, 8], Gabor filter-based

methods [48, 49], etc., which are highly based on prior assumption and unable to represent complex venous features. (2) Traditional machine learning algorithms. The traditional machine learning algorithms use shallow learning algorithms to model vein features, including SVM [19], PCA [20], K-means [21], Sparse Representation (SR) [22], Low-Rank Representation (LRR) [23]. The expression ability of these algorithms is limited so they are not well adapted to complex venous data.

B. Deep learning-based Vein Recognition Algorithms

Deep learning automatically learns features from a large amount of data by constructing a multi-layer neural network. It has strong representation ability and can deal with complex high-dimensional data. For example, Das et al. [15] proposed a CNN for finger vein recognition, Yang et al. [17] then proposed FVRASNet, which integrated vein recognition tasks and anti-spoofing tasks into a unified CNN model. In 2021, Qin et al. [24] proposed a CNN and a multi-scale multi-direction GAN-based data augmentation method for single-sample palm vein recognition. In the same year, to reduce the computational power consumption, Shen et al. [25] proposed a lightweight CNN for finger vein recognition. In 2023, Qin et al. [26] proposed a Label-Enhancement Multi-Scale vision Transformer (LE-MSVT) for palm vein recognition, In 2024, Qin et al. [27] proposed an Interactive Vein Transformer (IVT) to extract robust vein features and investigate an Attention-based Label Enhancement (ALE) approach to learn the label distribution for vein classification.

C. Mamba-based Algorithms

In 2023, Gu et al. [32] first proposed an end-to-end network architecture *i.e.* Selective State Space Model (named Mamba), which had the advantages of fast inference speed and linear complexity and outperformed Transformer's performance on many sequence tasks. In 2024, Zhu et al. [30] proposed Vision Mamba which introduced the Mamba model into the field of computer vision for the first time, its bidirectional Mamba scanning mechanism enabled Vision Mamba to achieve prominent performance on image classification and semantic segmentation tasks. Subsequently, various variants of Vision Mamba appeared. For example, Liu et al. [50] proposed VMamba which introduced a cross-scan module to extract global features. Huang et al. [33] proposed LocalVim, which introduced the local window scanning strategy to effectively capture local features, while maintaining the original global dependency representation ability of Mamba.

D. Neural Architecture Search Algorithms

Neural Architecture Search (NAS) is an automated network architecture learning approach to reduce the cost of heavy network design and improve the model's performance on specific tasks. Bergstra et al. [51] proposed a random search algorithm to uniformly sample within a given range of hyperparameters. Zoph et al. [39] first proposed a reinforcement learning-based neural network architecture search method. In

2020, Guo et al. [42] propose a single-path, one-shot NAS method using uniform sampling. The method simplifies the NAS process by training a supernet that can efficiently sample and evaluate subnets, solving the slow convergence and high computational cost associated with traditional NAS techniques. In 2021, Chen et al. [52] proposed a hierarchical network search algorithm with the evolutionary algorithm to search for the optimal Vit architecture from two levels. In the same year, Chen et al. [45] proposed a weight entanglement strategy that allows different candidate Transformer blocks to share weights, which enables more efficient searching of Vit models. In 2022, Su et al. [53] developed a new cyclic weight-sharing mechanism for token embedding in Vit. In 2023, Qin et al. [44] proposed a neural architecture search method based on attention gated recurrent unit to automatically search the optimal network architecture for the finger vein recognition task, introducing NAS technology into the field of vein recognition for the first time.

III. MAMBA PRELIMINARIES

A. State Space Models

The State Space Model (SSM) [54] is a mathematical model used to describe and analyze the behavior of the dynamical system. In the field of deep learning, state space models are used to process sequential data, such as time series analysis, natural language processing and video understanding. Long-term dependencies in the data can be better captured by mapping sequential data into state space. Given a one-dimension input sequence $x(t) \in \mathbb{R}^D$ and output $y(t) \in \mathbb{R}^D$, state space models use a set of equations to represent the relationship between them as Eq. (1).

$$\begin{aligned} h'(t) &= \mathbf{A}h(t) + \mathbf{B}x(t) \\ y(t) &= \mathbf{C}h(t) \end{aligned} \quad (1)$$

where $h(t) \in \mathbb{R}^V$ is a state space that stores the state of the system at time t and V is the size of it, $\mathbf{A} \in \mathbb{R}^{D \times V}$ is a state transition matrix, which describes how the state changes with time. $\mathbf{B} \in \mathbb{R}^{D \times 1}$ is the input control matrix, which describes how the external input affects the change of the state space. $\mathbf{C} \in \mathbb{R}^{D \times 1}$ is the output matrix, which describes how the state space is mapped to the output space.

This system is continuous, so it needs to be discretized before it is provided to the computer. Concretely, the system is discretized by using a zero-order hold (ZOH) assumption as shown in Eq. (2), it introduces a specific parameter $\Delta \in \mathbb{R}^D > 0$ which represents the step size to transform the continuous parameters (\mathbf{A}, \mathbf{B}) into a discrete form $(\bar{\mathbf{A}}, \bar{\mathbf{B}})$.

$$\begin{aligned} \bar{\mathbf{A}} &= e^{\Delta \mathbf{A}} \\ \bar{\mathbf{B}} &= (\Delta \mathbf{A})^{-1} (e^{\Delta \mathbf{A}} - I) \cdot \Delta \mathbf{B}. \end{aligned} \quad (2)$$

After the discretization, Eq. (1) can be rewritten as Eq. (3):

$$\begin{aligned} h'(t) &= \bar{\mathbf{A}}h(t) + \bar{\mathbf{B}}x(t) \\ y(t) &= \mathbf{C}h(t) \end{aligned} \quad (3)$$

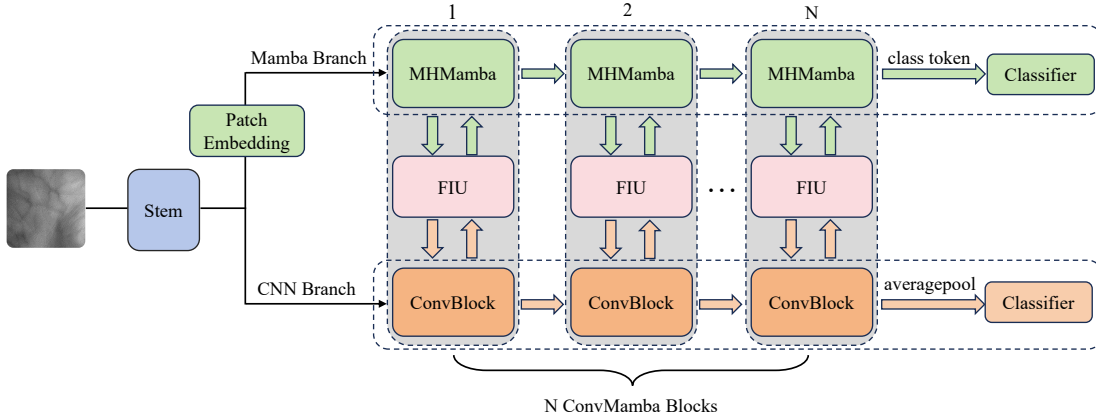


Fig. 1: The framework of the proposed Global-local Vision Mamba (GLVM). The Global-local Vision Mamba employs a dual-branch hybrid architecture which consists of a stem block, a patch embedding layer, N ConvMamba blocks, and two classifiers.

Finally, The sequence operation of the state space model can be transformed into a convolution operation by designing an appropriate convolution kernel, as shown in Eq. (4):

$$\begin{aligned} \bar{\mathbf{K}} &= (C\bar{B}, C\bar{A}\bar{B}, \dots, C\bar{A}^q\bar{B}, \dots, C\bar{A}^{Q-1}\bar{B}) \\ y &= x * \bar{\mathbf{K}} \end{aligned} \quad (4)$$

where $\bar{\mathbf{K}} \in \mathbb{R}^Q$ represents the convolution kernel of SSM. This greatly speeds up the computation of the state space model because convolution can be calculated in parallel in the computer.

B. Selective State Space Models

The parameters $(\mathbf{A}, \mathbf{B}, \mathbf{C})$ of the traditional state space model (usually refers to **S4** [31]) are linear time-invariant, *i.e.*, they do not change with the input. Therefore, **S4** cannot perform contextual content awareness and reasoning well due to this limitation. To solve this problem, Selective State Space Model (named **S6** or **Mamba** [32]) appeared, which introduces a dynamic selection mechanism that makes the \mathbf{B} , \mathbf{C} , and Δ depend on the input, so that the model can adaptively adjust its parameters according to the input. Concretely, Given the input sequence $x \in \mathbb{R}^{L \times D}$, $A \in \mathbb{R}^{D \times V}$ consistent with **S4**, Mamba calculates $\mathbf{B} \in \mathbb{R}^{L \times V}$, $\mathbf{C} \in \mathbb{R}^{L \times V}$, $\Delta \in \mathbb{R}^{L \times D}$ by Eq. (5):

$$\begin{aligned} \mathbf{B} &= \text{Linear}_B(x) \\ \mathbf{C} &= \text{Linear}_C(x) \\ \Delta &= \text{SoftPlus}_\Delta(\text{Linear}_\Delta(x) + \text{bias}) \end{aligned} \quad (5)$$

IV. METHODOLOGY

A. Global-local Vision Mamba Framework

Convolutional Neural Networks (CNNs) are good at extracting local features. However, it is difficult to capture global representations due to the local receptive field [28, 55]. Thanks to the state space model structure, Vision Mamba [30, 33] significantly enlarged receptive fields, constituting global representations with long-distance feature dependencies and showing better performance than Transformer in some applied fields. To extract global and local vein feature representation,

we combine CNN with the Mamba model and design a dual-branch hybrid architecture named Global-local Vision Mamba (GLVM). As shown in Fig. 1, GLVM includes three branches, *i.e.* CNN, Feature Interaction Unit (FIU), and multi-head Mamba (MHMamba) branches. The CNN branch includes N ConvBlocks and a classifier while the MHMamba branch includes N MHMamba blocks and a classifier. Additionally, a Feature Interaction Unit (FIU) branch is employed to fuse the features of the CNN branch and the MHMamba branch. In the CNN branch, a feature pyramid structure is employed to extract compact features, where the size of the feature map is reduced to $\frac{1}{2}$ of the size of the previous stage, and the number of feature channels is gradually increased by a factor of 2 at each stage in the forward process, the feature maps in the last layer are subjected to the max pooling operation and the resulting feature map is fed to a classifier layer. In the MHMamba branch, there are N repeated MHMamba blocks, where the size of feature maps in each layer keeps the same. The class token in the last layer is forwarded to another classifier layer. In the training phase, we average the CrossEntropy losses from the two classifiers to update the gradient. In the testing phase, we compute the summation of the prediction score of the two classifiers as the final classification result. Our model architecture is detailed as follows.

(1) Stem. In the stem block, a 7×7 convolution with a stride of 2 is used to preliminarily extract the features. To reduce computational complexity and prevent overfitting, the spatial size of feature maps is reduced by a 3×3 max pooling layer with a stride of 2. For an input image $X \in \mathbb{R}^{C_0 \times H \times W}$, where C_0 is the number of channels, H and W is the width and height, the stem block transforms it from image space to feature space F_c^1 by Eq. (6):

$$F_c^1 = \text{MaxPool}_{3 \times 3}(\text{ReLU}(\text{BN}(\text{Conv}_{7 \times 7}(X)))) \quad (6)$$

where $F_c^1 \in \mathbb{R}^{C \times \frac{H}{4} \times \frac{W}{4}}$, C is the number of output channels, ReLU is an active function, BN is the batch normalization and $\text{Conv}_{k \times k}$ is a convolution operator with a kernel of $k \times k$.

(2) Patch Embedding. The patch embedding layer maps the 2D feature map F_c^1 into a series of 1D patch embeddings. Specifically, the feature maps F_c^1 are divided into L non-

overlapping patches with size $p \times p$ and the number of patches is $L = \frac{H}{p} \times \frac{W}{p}$. Then we compute the embeddings of resulting patches. To achieve this, we implement a convolution on different feature maps with D kernels of $p \times p$ at a stride of p by Eq. (7):

$$F_m^1 = \text{Transpose}(\text{Flatten}(\text{Conv}_{p \times p}(F_c^1))). \quad (7)$$

where $F_m^1 \in \mathbb{R}^{L \times D}$, *Transpose* denotes the matrix transpose operation, and *Flatten* operation transforms the 2D matrix into 1D vectors. In fact, D also represents the embedding dimensions. Finally, F_m^1 and F_c^1 are taken as the input of the first ConvMamba block.

(3) ConvMamba Block. As shown in Fig. 2, ConvMamba block consists of three branches: CNN branch, Feature Interaction Unit (FIU) branch, and Multi-head Mamba (MHMamba) branch, which are detailed as follows.

CNN Branch. The CNN branch includes 2 sub-convolution blocks, each of which consists of three convolution layers, followed by batch normalization and ReLU activation. Let F_c^i be the input feature maps of the i -th ConvMamba block in the CNN branch, the forward process is formulated as:

$$\tilde{F}_c^{i,1} = \text{DWConv}_{3 \times 3}(\text{Conv}_{1 \times 1}(F_c^i)) \quad (8)$$

$$\tilde{F}_c^{i,2} = \text{Conv}_{1 \times 1}(\text{Conv}_{1 \times 1}(\tilde{F}_c^{i,1}) + F_c^i) \quad (9)$$

$$\tilde{F}_m^{i+1} = \text{FIU}_2(F_m^{i+1}) \quad (10)$$

$$F_c^{i+1} = \text{Conv}_{1 \times 1}(\text{DWConv}_{3 \times 3}(\tilde{F}_c^{i,2} + \tilde{F}_m^{i+1})) \quad (11)$$

where *DWConv* represents the depthwise convolution, which can effectively reduce the amount of computation and the number of parameters, and improve the inference speed and operation efficiency of the model. *FIU*₂ represents the second module of the FIU, and F_m^{i+1} is the output of the MHMamba branch in the i -th ConvMamba block. Noted that we neglect the batch normalization and active function in Eqs. (8)-(11) for simplification.

Multi-head Mamba Branch. To improve the feature representation capacity of classic Mamba blocks [32], we design a Multi-head Mamba (MHMamba) block as shown in Fig. 3, which employs the multi-head strategy of Transformer [29] in addition to the multi-directional scanning strategy, and greatly improves the recognition accuracy of the Mamba branch. As shown in Fig. 2(a), F_m^i is the input of MHMamba branch in the i -th ConvMamba block and the feature map $\tilde{F}_c^{i,1}$ is the intermediate output of the first convolution block of the CNN branch in i -th ConvMamba block. F_m^i and $\tilde{F}_c^{i,1}$ are combined by Eq. (12):

$$\tilde{F}_m^i = F_m^i + \text{FIU}_1(\tilde{F}_c^{i,1}) \quad (12)$$

where *FIU*₁ is the first module of the feature interaction unit branch. The resulting embeddings $\tilde{F}_m^i \in \mathbb{R}^{L \times D}$ is taken as the input of the MHMamba block for the feature extraction and the computation process is shown in Eqs. (13)-(18):

$$\overline{F}_m^i = \text{Linear}(\text{RMSLN}(\tilde{F}_m^i)) \quad (13)$$

where *RMSLN* represents the Root Mean Square Layer Normalization [56], and *Linear* is a linear layer. Then, similar to Transformer, the resulting embeddings $\overline{F}_m^i \in \mathbb{R}^{L \times (E \times D)}$

(E is the dimension expansion ratio) are split into different heads $H_t \in \mathbb{R}^{L \times D_h}$, $t = 1, 2, \dots, T$ by Eq. (14):

$$\Omega_m^i = \text{Split}(\overline{F}_m^i) = \{H_1, H_2, \dots, H_T\} \quad (14)$$

where T is the number of heads and D_h is the dimension of each head. For all heads H_t , $t = 1, 2, \dots, T$, we map them into J directions by Eq. (15), respectively.

$$H_t = \text{MultiScan}(H_t) = \{H_t^1, H_t^2, \dots, H_t^J\} \quad (15)$$

where *MultiScan* is a 2D scanning method, which scans the input along different directions, *e.g.* vertical, flipped vertical, horizontal, and flipped vertical, as shown in Fig. 3(c). $H_t^j \in \mathbb{R}^{L \times D_h}$ represents the j -th direction of the t -th head and is further input to the Mamba module (Fig. 3(b)) to learn the global feature by Eq. (16):

$$H_t^j = \text{SSM}(\text{Conv}_{1 \times 1}(H_t^j)) \cdot \text{SiLU}(H_t^j) \quad (16)$$

where *SSM* is the selective state space model [32], and *SiLU* is an activation function [57]. We concatenate the heads along the same direction by Eq. (17):

$$\begin{aligned} \hat{F}_m^i &= \text{Concat}\{H_1^1, H_2^1, \dots, H_T^1\} \\ &+ \text{Concat}\{H_1^2, H_2^2, \dots, H_T^2\} \\ &+ \dots + \text{Concat}\{H_1^J, H_2^J, \dots, H_T^J\} \end{aligned} \quad (17)$$

The resulting embeddings \hat{F}_m^i are forwarded to a linear layer, which is computed by Eq. (18):

$$F_m^{i+1} = \text{Linear}(\hat{F}_m^i) \quad (18)$$

Feature Interaction Unit Branch. In this section, we design a Feature Interaction Unit (FIU) to align the spatial information of the CNN branch's local features and the MHMamba branch's global representations in a complementary so that they can be fused. As shown in Fig. 2, FIU consists of two sub-modules, *i.e.* *FIU*₁ and *FIU*₂.

The $\tilde{F}_c^{i,1} \in \mathbb{R}^{C_1 \times H_1 \times W_1}$ in Eq. (8) is the input of *FIU*₁ and the $F_m^i \in \mathbb{R}^{L \times D}$ in Eq. (12) is the input of MHMamba branch. *FIU*₁ first aligns the channel numbers of $\tilde{F}_c^{i,1}$ and F_m^i to get $\hat{F}_c^{i,1} \in \mathbb{R}^{D \times H_1 \times W_1}$ through a 1×1 convolution layer, and then aligns the spatial resolution information of $\hat{F}_c^{i,1}$ and F_m^i to get $\overline{F}_c^{i,1} \in \mathbb{R}^{L \times D}$ through an average pool layer followed by flatten and transpose operations. The resulting feature is regularized and activated by BatchNorm and GeLU functions [57]. The forward process of *FIU*₁ is formulated as:

$$\begin{aligned} \hat{F}_c^{i,1} &= \text{Conv}_{1 \times 1}(\tilde{F}_c^{i,1}) \\ \overline{F}_c^{i,1} &= \text{AveragePool}(\text{Transpose}(\text{Flatten}(\hat{F}_c^{i,1}))) \\ \overline{F}_c^{i,1} &= \text{GeLU}(\text{LN}(\hat{F}_c^{i,1})) \end{aligned} \quad (19)$$

The alignment feature $\overline{F}_c^{i,1}$ will be fused with F_m^i by Eq. (12), as shown in Fig. 2.

In addition, the input of *FIU*₂ is $F_m^{i+1} \in \mathbb{R}^{L \times D}$ in Eq. (18) and the CNN branch's intermediate feature maps is $\tilde{F}_c^{i,2} \in \mathbb{R}^{C_2 \times H_2 \times W_2}$ in Eq. (9). Similarly, *FIU*₂ first aligns the channel numbers of F_m^{i+1} and $\tilde{F}_c^{i,2}$ to get $\hat{F}_m^{i+1} \in \mathbb{R}^{C_2 \times h \times w}$ ($h = w = \frac{H}{p} = \frac{W}{p}$) through transpose, reshape operations and a 1×1

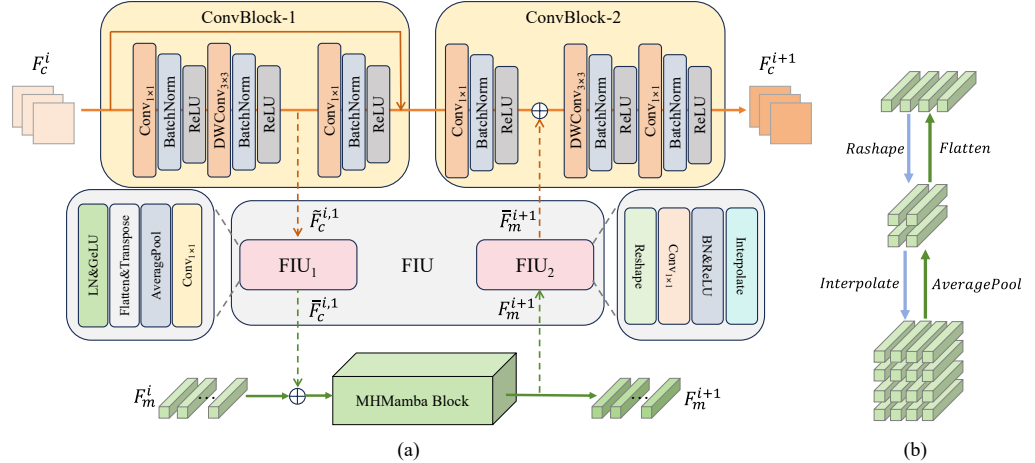


Fig. 2: The architecture of ConvMamba block. (a) Each ConvMamba block consists of a MHMamba block, a feature interaction unit, and a Convolutional block, each sub-convolution block includes 3 convolution layers followed by the BatchNorm regularization and ReLU activation. (b) The basic operations in a Feature Interaction Unit, e.g., Flatten and Averagepool.

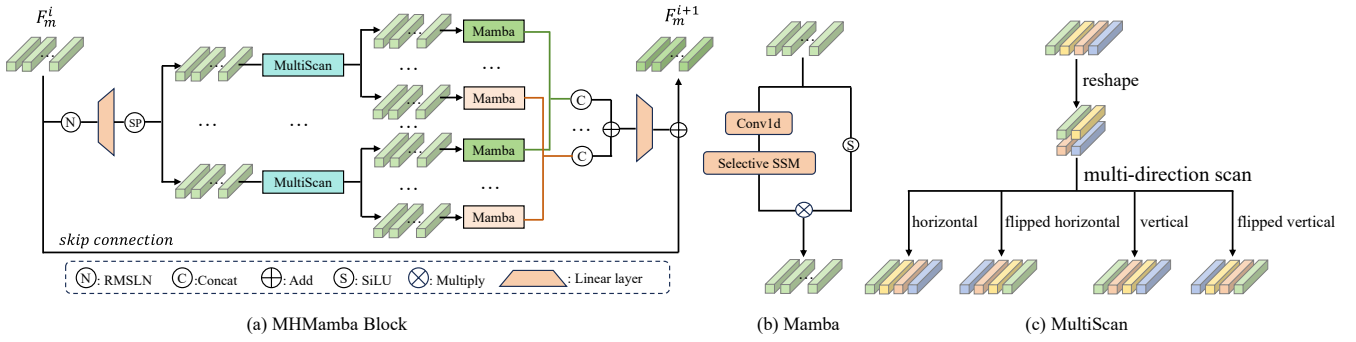


Fig. 3: The architecture of Multi-head Mamba (MHMamba) block.

convolution layer followed by BN regularization and $ReLU$ activation, and then aligns the spatial resolution information of \hat{F}_m^{i+1} and $\hat{F}_c^{i,2}$ to get $\bar{F}_m^{i+1} \in \mathbb{R}^{C_2 \times H_2 \times W_2}$ by the *Interpolate* operation. The forward process of *FIU*₂ is formulated as:

$$\begin{aligned} \hat{F}_m^{i+1} &= Conv_{1 \times 1}(Reshape(Transpose(F_m^{i+1}))) \\ \hat{F}_m^{i+1} &= ReLU(BN(\hat{F}_m^{i+1})) \\ \bar{F}_m^{i+1} &= Interpolate(\hat{F}_m^{i+1}) \end{aligned} \quad (20)$$

The alignment feature \bar{F}_m^{i+1} will be fused with $\hat{F}_c^{i,2}$ by Eq. (11).

B. Search space of Global-local vision Mamba.

The search space consists of the global architecture of global-local vision Mamba and local detail architecture of each Multi-head Mamba Block as shown in Tab. I.

(1) Global search space. The global architecture hyperparameter determines the scale of the network, which affects the size of all local modules and plays a key role in the final performance of the model. Suppose that there are N ConvMamba blocks, the embedding dimension in the patch embedding layer is D , and the number of channels in the stem layer is C . As listed in Tab. I, the N , C , and D are sampled into discrete values. Let S_1 , S_2 , S_3 represent the total

TABLE I
The search space of our GLVM

Stage	Hyperparameter	Symbol	(Min, Max, Interval)
Global	Depth	N	(6, 12, 3)
	Channel Num	C	(32, 128, 32)
	Embed Dim	D	(128, 384, 64)
Local	Head Num	T	(2, 6, 2)
	Expand Ratio	E	(1, 2, 0.5)
	State Size	V	(16, 48, 16)

candidate numbers of the hyperparameters N , C , and D respectively, we can get the search sets $\mathcal{N}_1 = \{N_1, N_2, \dots, N_{S_1}\}$, $\mathcal{N}_2 = \{D_1, D_2, \dots, D_{S_2}\}$, and $\mathcal{N}_3 = \{C_1, C_2, \dots, C_{S_3}\}$ of N , C , D respectively. The final global candidate architecture search set is $\mathcal{N}_G = \mathcal{N}_1 \times \mathcal{N}_2 \times \mathcal{N}_3$, where \times represents the Cartesian product.

(2) Local search space. The local architecture hyperparameters are associated with local detail architecture in the MHMamba block (Fig. 3(a)). The search space of detailed architecture includes the dimension expansion rate E , the number of heads T , and the size of the state space V in SSM (section III-B). Similarly, we discretize the continuous space into different values and the candidate numbers in E , T and V are S_4 , S_5 , and S_6 . As a result, the candidate sets

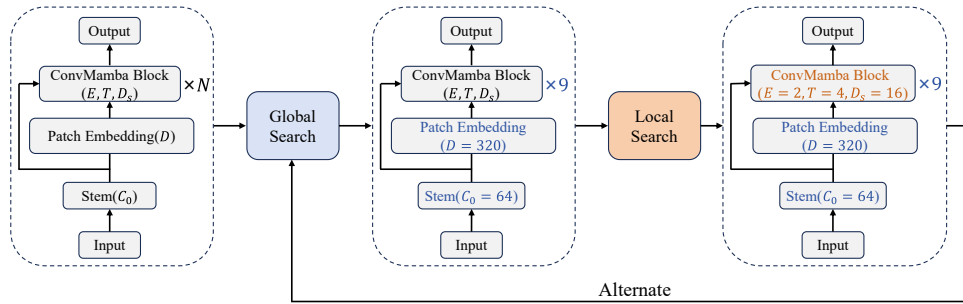


Fig. 4: Framework of the GLANAS. We split the search space into two parts, global space and local space, and alternately perform a two-stage search, with each stage of the search employing a weight entanglement strategy to sample subnets from the supernet.

of E , T , V can be denoted by $\mathcal{N}_4 = \{E_1, E_2, \dots, E_{S_4}\}$, $\mathcal{N}_5 = \{T_1, T_2, \dots, T_{S_5}\}$ and $\mathcal{N}_6 = \{V_1, V_2, \dots, V_{S_6}\}$ respectively. For a MHMamba block $b_n \in \{b_1, b_2, \dots, b_n, \dots, b_N\}$, the inner search sets are \mathcal{N}_4^n , \mathcal{N}_5^n and \mathcal{N}_6^n . The overall search set of block b_n is $\mathcal{S}_n = \mathcal{N}_4^n \times \mathcal{N}_5^n \times \mathcal{N}_6^n$ and the final local search space is $\mathcal{N}_L = \mathcal{S}_1 \times \mathcal{S}_2 \times \dots \times \mathcal{S}_N$.

(3) Search space size. For each MHMamba block, there are $S_4 S_5 S_6$ candidate architectures. In our search space, different MHMamba blocks have different architectures. Considering the global and local architecture hyperparameters, the search space size of the global architecture is $S_1 S_2 S_3$, the search space size of the local architecture is $(S_4 S_5 S_6)^{N_{S_1}}$, and the final search space contains $S_2 S_3 \sum_{i=1}^{S_1} (S_4 S_5 S_6)^{N_i}$ candidate networks. As listed in Tab. I, $S_1 = 3$, $S_2 = 4$, $S_3 = 5$, $S_4 = 3$, $S_5 = 3$, $S_6 = 3$, and $N_1 = 6$, $N_2 = 9$, $N_3 = 12$, so there are $(S_2 S_3)[(S_4 S_5 S_6)^6 + (S_4 S_5 S_6)^9 + (S_4 S_5 S_6)^{12}] \approx 3 \times 10^{18}$ candidate networks, which is an extremely huge search space. The mainstream fast architecture search methods such as one-shot NAS with weight sharing [42] show poor performance in such a huge search space because it selects one candidate network for weight updating in each training iteration. However, due to the huge search space, the weights of most candidate architectures are not updated after completing supernet training, resulting in a low correlation between the retrained subnet and the subnet sampled from the supernet, so the architectures searched by using supernet are unreliable. To solve the problem, we propose a Global-local Alternating Neural Architecture Search (GLANAS) method to get the optimal global and local network architecture with suitable memory requirements.

C. Global-local Alternating Neural Architecture Search

The section IV-B has defined the search space of our proposed architecture, which consists of global architecture search space and local module search space. In this section, we design a novel architecture search method named Global-local Alternative Neural Architecture Search (**GLANAS**) as shown in Fig. 4, which contains three stages: global search, local search, and alternative search.

(1) Global Search. At the global search stage, we initial and fix the local architecture parameters in the ConvMamba block to optimize global architecture parameters. The Weight Entanglement method [45] is applied to find the optimal global architecture. The global search space \mathcal{N}_G is encoded in a supernet $\mathcal{R}(\mathcal{N}_G, W)$, where W denotes the weight of the

supernet. Let β be the subnets that are sampled from the supernet \mathcal{R} , and the W is shared among all the candidate architectures $\beta \in \mathcal{N}_G$. The One-Shot NAS method is usually a two-stage optimization problem. At first stage, the weight W of the supernet \mathcal{R} is optimized by Eq. (21):

$$W_{\mathcal{N}_G} = \arg \min_W \mathcal{F}_{train}(\mathcal{R}(\mathcal{N}_G, W)), \quad (21)$$

where \mathcal{F}_{train} is the loss function on the training dataset. Then the one-shot method samples subnets β from the supernet \mathcal{R} . The second phase aims to search optimal subnet β_* based on the accuracy of all subnets $\beta \in \mathcal{N}_G$ on validation set, which is computed by Eq. (22):

$$\beta_* = \arg \max_{\beta \in \mathcal{N}_G} \text{Acc}_{val}(\mathcal{R}(\beta, W_{\mathcal{N}_G}(\beta))), \quad (22)$$

where $W(\beta)$ is the weight of sampled subnet β which inherits from the supernet weight \mathcal{R} and Acc_{val} denotes the accuracy of the subnet β on the validation dataset. After the global search, we obtain the optimal global architecture hyperparameters $\beta_* = (N_*, C_*, D_*)$, where $*$ represents the optimal choice.

(2) Local Search. After obtaining the optimal global architecture hyperparameters at the global search stage, we fix such parameters and search the local module architectures (*i.e.* all ConvMamba blocks). Similarly, the Weight Entanglement method [45] is employed to optimize the local module architecture hyperparameters. The difference between global search and local search is changed the search space. Correspondingly, we finally get the optimal local module architecture $\gamma_* = ((T_*^1, E_*^1, V_*^1), (T_*^2, E_*^2, V_*^2), \dots, (T_*^{N_*}, E_*^{N_*}, V_*^{N_*}))$.

(3) Alternative search. After the first global search and local search, we obtain the global architecture and the local module detail. We can think that the latter may be optimal relative to the former, but we can not guarantee that the former is optimal relative to the latter. Therefore, we fix the local module hyperparameters to perform global search again, the final network architecture is obtained by alternating this process for K times.

The proposed global-local alternating search method has the following advantages compared with existing NAS methods [42, 44, 45]. First, the huge search space is split into two smaller search spaces. Specifically, the size of original space is $S_2 S_3 \sum_{i=1}^{S_1} (S_4 S_5 S_6)^{N_i}$, which is divided into two smaller spaces $S_1 S_2 S_3$ and $(S_4 S_5 S_6)^{N_{S_1}}$ by our approach and the final search space size is $S_1 S_2 S_3 + (S_4 S_5 S_6)^{N_{S_1}} \approx 1.5 \times 10^{17}$. Therefore, the new search space is reduced to less than 20

times the original search space. As the final search space falls into the effective search space range of existing NAS methods, making it easier for the Weight Entanglement method [45] to obtain a better model. Second, our alternate search scheme ensures that a highly compatible and performant architecture can be found in the huge search space.

V. EXPERIMENTS AND RESULTS

To verify the performance of our approach, we carry out rigorous experiments on three public vein databases. In experiments, we compare the proposed approach with existing approaches, including six advanced vein recognition models (PVCNN [24], FVCNN [15], LWCNN [25], FVRASNet [17], LE-MSVT [26], ALE-IVT [27]) and four the state of the art models (ResNet50 [10], Vim [30], Vit [11], LocalVim [33]). Also, the existing NAS methods, such as Random Search [51], SPOS [42], AutoFormer [45], AGNAS [44] are repeated to demonstrate the effectiveness of our proposed GLANAS method.

A. Databases

(1) TJU_PV: The Tongji University Palm Vein database [58] includes 12,000 palm vein images (300 subjects \times 2 palms \times 10 images \times 2 sessions), captured from 300 subjects (*i.e.* 600 palms) at two separate sessions with an average time interval of about two months. Finally, there are 600 categories with 20 images in each category by treating each palm as a category.

(2) VERA_PV: The VERA Palm Vein database [59] contains 2200 images (110 subjects \times 2 palms \times 5 images \times 2 sessions) collected from 110 subjects at two separate sessions. Each subject provides two palms, and five images per palm are captured in each session. So there are 220 categories with 10 images in each category by treating each palm as a category.

(3) HKPU_PV: The Hong Kong Polytechnic University's multispectral Palm Vein database [60] consists of 6,000 (250 subjects \times 2 palms \times 6 images \times 2 sessions) palm-vein images captured from 250 individuals at two separate sessions with an average time interval of nine days. If we treat each palm as a category, there are 500 categories, each of which provides 12 images.

Palm vein images from the three databases are captured in a contact or contactless way. Generally, there are some translations and rotations which result in mismatching. Also, the background region in capturing images can not provide any discrimination information. Therefore, all the Region of Interest (ROI) images were extracted from the original images based on the preprocessing approach [61] and normalized to the same direction, as shown in Fig. 5.

B. Experimental Settings

(1) Database Settings. To test our approach, we split each palm database into three sets: training set, validation set, and testing set. The model is trained on the training set, the validation set is used for model tuning, and the test set is used to evaluate the final performance of the model. All the databases are collected from two sessions, the first session images are

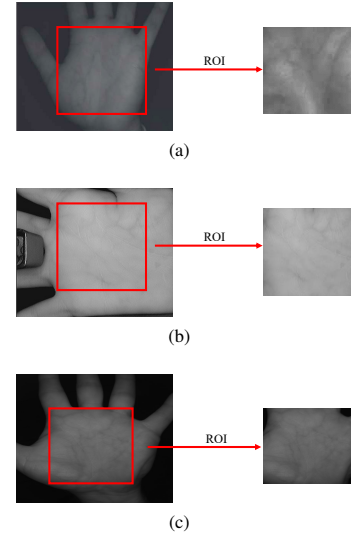


Fig. 5: Preprocessing results on three databases. Original palm image and ROI on (a) TJU_PV database, (b) HKPU_PV database, and (c) VERA_PV database.

used as the training set and the second session images are divided into the validation and testing sets. Specifically, for the TJU_PV database, there are 12,000 (600 palms \times 10 images \times 2 sessions) images from 600 palms. The images from the first session are employed for training and the training set contains 6000 images (600 classes \times 10 images). For the 10 images for each class in the second session, we use the first 5 images for validation and the last 5 for testing. As a result, there are 3,000 images (600 classes \times 5 images) in the validation set and 3,000 images (600 classes \times 5 images) in the testing set. Similarly, for the VERA_PV database, the training set includes 1,100 images (220 classes \times 5 images), and there are 440 images (220 classes \times 2 images) in the validation set and 660 images (220 classes \times 3 images) in the testing set. For the HKPU_PV database, there are 3,000 images (500 classes \times 6 images) in the training set, 1,500 images (500 classes \times 3 images) in the validation set and 1,500 images (500 classes \times 3 images) in the testing set. Due to the limited number of vein database samples, the deep learning-based vein recognition model is very susceptible to overfitting, we perform data augmentation operations for each database including geometric transformations (rotation, scaling, flipping, cropping), color enhancement transformations (contrast, brightness, hue, and saturation) and the classical mix-up method [62].

(2) Training Hyperparameters. The adaptive moment estimation with weight decay (AdamW) [63] optimizer is employed to model parameter optimisation. The initial learning rate is set to 0.001 which has a warmup epoch number of 5, it will eventually reduce to 0.0001 with a cosine scheduler, the weight decay is 0.05, and the minibatch sizes are set to 60, 50, and 40 for TJU_PV, VERA_PV, and HKPU_PV databases respectively. The maximum number of training epochs is set to 500. All experiments are implemented on PyTorch with an NVIDIA Tesla A100 80G GPU.

(3) Evaluation Metrics. In our experiment, the top-1 recognition accuracy (ACC) and equal error rate (EER) are employed to evaluate the performance of all vein recognition

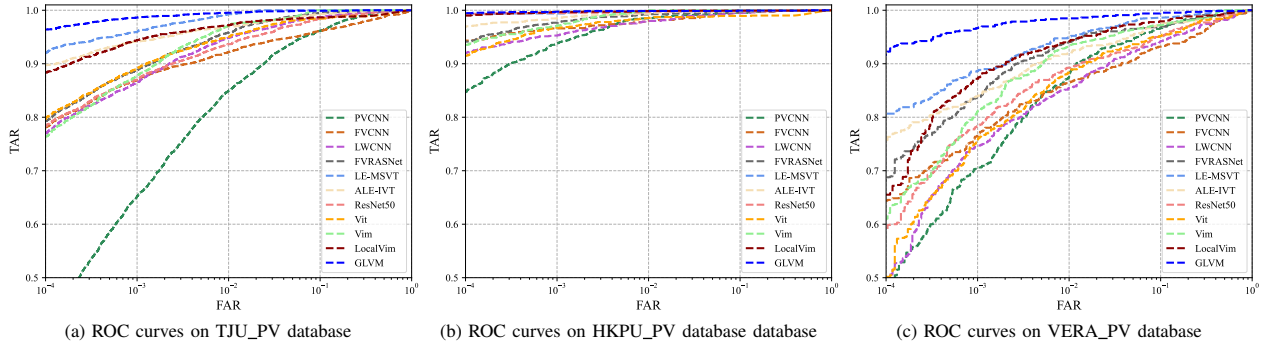


Fig. 6: ROC curves for different models on three public vein databases.

approaches effectively. Note that the EER is the error rate when the false accepted rate (FAR) is equal to the false rejected rate (FRR). Furthermore, The ROC curve provides a comprehensive view of the model's performance at all thresholds and is plotted by FAR against the true accepted rate (TAR=1-FRR). The area under the ROC curve is an important performance metric that quantifies a model's recognition ability, the larger the area implies that the model achieves the better the recognition performance. Thus, we plot ROC curves for all methods to test their performance.

C. Performance of Global-local Vision Mamba

In this section, we evaluate the performance of the proposed Global-local Vision Mamba (GLVM) in terms of recognition performance improvement. In experiments, the state of arts (*i.e.* PVCNN [24], FVCNN [15], LWCNN [25], FVRASNet [17], LE-MSVT [26], ALE-IVT [27], ResNet50 [10], Vim [30], Vit [11], LocalVim [33]) are implemented for comparison. All models are trained end-to-end from scratch. In this experiment, the architecture hyperparameter in Table I for our GLVM is determined by our prior knowledge. Specifically, we set $N = 12$, $C = 64$, $D = 32$, $T = 4$, $E = 2$, and $V = 16$ to achieve good performance. We report the recognition accuracy and equal error rate (EER) to verify the performance of our approach. The experimental results of various approaches on the three public databases are illustrated in Table II. The corresponding ROC curves are shown in Fig. 6.

TABLE II
Recognition accuracy (%) and EER (%) of various approaches on three public databases.

Approach	TJU_PV		HKPU_PV		VERA_PV	
	ACC	EER	ACC	EER	ACC	EER
PVCNN[24]	80.52	3.57	95.80	1.66	85.30	3.19
FVCNN[15]	86.43	3.03	94.87	1.82	79.58	4.58
LWCNN[25]	85.64	3.09	93.47	1.73	80.76	4.74
FVRASNet[17]	87.33	2.29	94.67	0.85	89.12	2.81
LE-MSVT[27]	92.57	1.23	96.87	0.72	84.55	3.63
ALE-IVT[26]	93.63	0.87	99.13	0.26	91.52	2.09
ResNet50[10]	90.23	1.47	98.93	0.39	89.55	2.48
Vit[11]	84.40	3.26	94.00	1.05	77.12	4.83
Vim[30]	85.57	2.86	95.40	0.99	82.79	3.92
LocalVim[33]	91.47	1.34	98.47	0.32	86.97	2.76
GLVM	95.57	0.47	99.40	0.20	94.23	0.62
Gain	+1.94	-0.40	+0.27	-0.06	+2.71	-1.47

From the experimental results in Table II, we can observe that our approach outperforms the existing approaches considered in our work and achieves the highest recognition accuracy and lowest verification errors. Specifically, our GLVM performs the accuracy of 95.57%, 99.40% and 94.23% on TJU_PV, HKPU_PV, and VERA_PV databases, respectively, which are 1.94%, 0.27% and 2.71% higher than the best method among all the compared methods. Also, our method achieves the lowest equal error rates, 0.47%, 0.20%, and 0.62% on the three databases and outperforms the previous best approaches with an error reduction of 0.40%, 0.06%, and 1.47%. From Fig. 6, we also observe that our method achieves the highest recognition accuracy at different FARs. Such excellent performance may be attributed to the following facts: 1) The Structured State Space Models (SSMs) in Mamba achieve linear complexity and render a global receptive field, and have shown superior performance compared to Transformer in some visual classification tasks [30, 33]. Also, we investigate a multi-head Mamba to further improve the feature representation capacity of Mamba, as shown in Fig. 3. 2) Our ConvMamba block (Fig. 2) in GLVM consists of Mamba module and CNN module. The convolution operators are capable of extracting local features and the Mamba aims to capture global representations [30]. Therefore, our approach exploits the complementarities of local features and global representations to achieve robust feature representation for vein recognition. In our experiments, for single branch-based approaches *i.e.* single CNN (PVCNN [24], FVCNN [15], LWCNN [25], FVRASNet [17], ResNet50 [10]), single Transformer (MSVT [26], Vit [11]) and single Mamba-branch (Vim [30], LocalVim [33]) show poor performance in our experiments. This may be attributed to the facts: 1) CNNs can effectively capture local features by sharing weights and local perception, but it is difficult to capture long-distance relationships among visual elements due to their limited receptive field [28, 55]; 2) By contrast, the Transformer or Mamba enlarges the receptive fields, constituting global representations with long-distance feature dependencies [28, 30, 33, 55] but they ignore local feature details. So, ALE-IVT [27] combines the CNN and Transformer to learn local features and global representations, thereby achieving higher recognition performance.

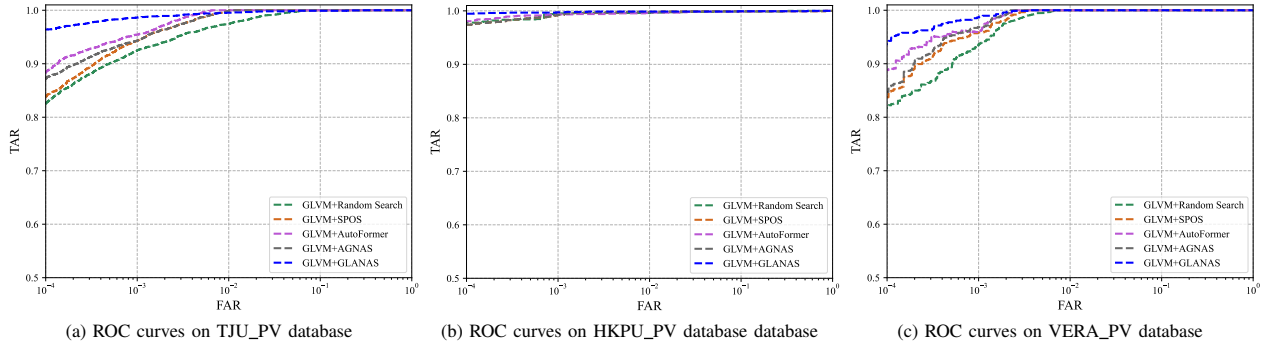


Fig. 7: ROC curves for different NAS methods on three public vein databases.

D. Performance of GLANAS

To further investigate the performance, we compare the proposed GLANAS approach with existing NAS approaches, *i.e.* Random Search [51], SPOS [42], AutoFormer [45] and AGNAS [44]. For fair comparison, all search methods are employed to search the hyperparameter of GLVM with same search space (Table I). The experimental results have been listed in Table III and the ROC curves are shown in Fig. 7.

TABLE III

Performance comparisons between different search methods on three public databases.

Approach	TJU_PV		HKPU_PV		VERA_PV	
	ACC	EER	ACC	EER	ACC	EER
GLVM+Random Search[51]	94.90	0.55	99.34	0.27	94.13	0.75
GLVM+ SPOS[42]	95.63	0.48	99.47	0.31	94.53	0.68
GLVM+AutoFormer[45]	95.78	0.44	99.54	0.22	94.79	0.59
GLVM+AGNAS[44]	95.74	0.42	99.45	0.16	94.68	0.65
GLVM+GLANAS	96.84	0.27	99.63	0.07	95.87	0.48
Gain	+1.06	-0.15	+0.09	-0.09	+1.08	-0.11

From the experimental results (Table III and Fig. 7), our GLVM with GLANAS achieves a significant accuracy improvement than other approaches, *i.e.*, an improvement of 1.06%, 0.09%, and 1.08% *w.r.t* the second best approaches on the TJU_PV, HKPU_PV, and VERA_PV databases, respectively. Meanwhile, applying GLANAS to search the architecture of GLVM can reduce the equal error rate by 0.15%, 0.09%, and 0.11% on the three databases, respectively. In experiments, Random Search [51] achieves poor performance among all search approaches. This is because it is difficult to choose a better architecture in such a huge search space due to its uncertainty. SPOS [42] construct a simplified supernet, where all subnets share the weights in their own separate modules, so such an architecture search is fast and suitable for large datasets and achieves good performance. Similarly, reinforcement learning is proposed to sample a subnet from supernet [44] for vein recognition. However, the weights of its different blocks are independent in the same layer, which results in slow convergence and low performance. By contrast, the weight entanglement strategy of AutoFormer [45] enables different Transformer blocks to share weights for their common parts in each layer and achieve higher performance than SPOS [42]. However, as described in Section IV-B, the search space is huge for the GLVM, the retrained subnet and the subnet sampled from the supernet have a low correlation in

such a search space. Therefore, these single supernet-based architectures searched approaches [42, 44, 45] are unreliable. Our GLANAS divides the final search space into the effective search space range of existing NAS methods, which makes it easier for weight entanglement-based NAS [45] to obtain the better model.

In addition, compared the experimental results in Table II and Table III, we found that the resulting GLVM achieves better performance after automatically searching its architecture instead of manually selection. The reason is that existing NAS and our GLANAS optimize the architecture of our GLVM for different tasks, eliminating the risk of manually discarding optimal networks for classification. Similar conclusions have been demonstrated in recent works [44, 64].

E. Ablation Experiments

(1) GLVM Architecture Ablation. As shown in Fig. 2, the ConMamba block in GLVM consists of a Multi-head Mamba branch, a CNN branch, and a feature interaction unit branch. This experiment aims to investigate the impact of different components on performance. For the obtained architectures in Table IV, first, only the multi-head Mamba branch is retrained in the obtained architectures, which is represented by the multi-head Mamba branch. Secondly, we only retain the CNN branch and denote it as the CNN branch. Thirdly, we replace the multi-head Mamba in the multi-head Mamba branch with a single Mamba (original Mamba [30]), and the resulting model is denoted as the Single-head Mamba branch. Fourthly, we combine prediction scores of the CNN branch and multi-head Mamba branch and such a mechanism is a dual branch (no Feature Interaction Unit). Finally, the Feature Interaction Unit branch is utilized to fuse the CNN branch and multi-head Mamba branch and the resulting model is Dual branch + FIU (GLVM). All experimental results are illustrated in Table V, which implies that the integration of the Multi-head Mamba branch, CNN branch, and Feature Interaction Unit branch allows to achieve higher recognition performance. In addition, our multi-head Mamba outperforms single Mamba and achieves higher recognition accuracy.

TABLE IV
Searching architecture on three public databases.

Database	Global Architecture	Local Architecture											
		1	2	3	4	5	6	7	8	9	10	11	12
TJU_PV	(9,320,128)	(4,2,16)	(6,1.5,32)	(4,2,16)	(4,2.5,32)	(2,1.5,48)	(4,1,48)	(6,1,48)	(2,2,16)	(4,2.5,32)			
HKPU_PV	(9,256,64)	(2,1,48)	(2,2,32)	(2,2,48)	(4,1,5,16)	(4,1.5,48)	(2,2.5,48)	(4,1.5,16)	(2,1,32)	(4,2,16)			
VERA_PV	(6,192,64)	(4,2,32)	(4,2,16)	(4,1,16)	(2,2,16)	(4,1,48)	(4,1,16)						

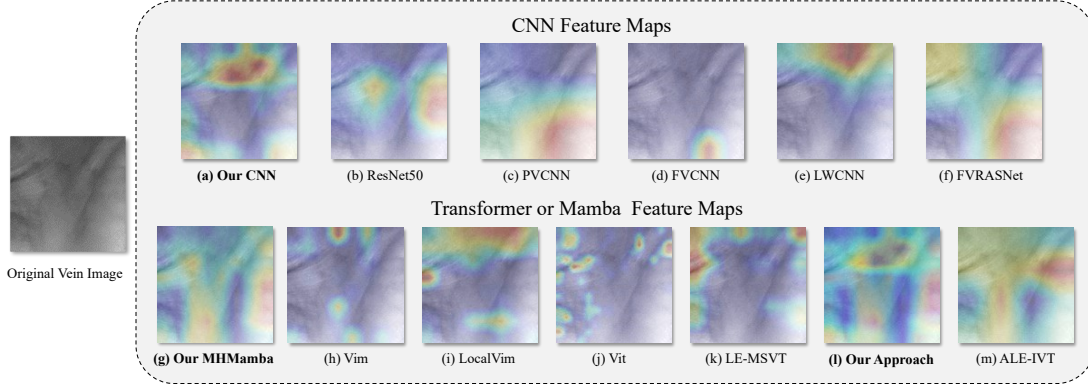


Fig. 8: Feature Heat maps in various methods by using the GradCAM method [65]. The heat maps from (a) Our CNN branch, (b) ReNet50 [10], (c) PVCNN [24], (d) FVCNN [15], (e) LWCNN [25], (f) FVRASNet [17], (g) Our MHMamba branch, (h) Vim [30], (i) LocalVim [33], (j) Vit [11], (k) LE-MSVT [26], (l) Our Approach, and (m) ALE-IVT [27].

TABLE V
Ablation experiment results of proposed GLVM on three public databases.

Approach	TJU_PV		HKPU_PV		VERA_PV	
	ACC	EER	ACC	EER	ACC	EER
Single-head Mamba branch	85.57	2.86	95.40	0.99	82.79	3.92
Multi-head Mamba branch	89.13	1.63	96.33	0.64	85.97	2.61
CNN branch	93.36	0.96	97.73	0.54	92.58	1.89
Dual branch	94.54	0.89	98.33	0.28	93.09	1.22
Dual branch + FIU (GLVM)	95.57	0.47	99.40	0.20	94.23	0.62

TABLE VI
Ablation experiment results of proposed GLANAS on three public databases.

Approach	TJU_PV		HKPU_PV		VERA_PV	
	ACC	EER	ACC	EER	ACC	EER
One stage searching	95.78	0.44	99.54	0.22	94.79	0.59
Two stage searching	96.27	0.36	99.58	0.14	94.83	0.56
Alternative searching (GLANAS)	96.84	0.27	99.63	0.07	95.30	0.48

(2) GLANAS Ablation. Our GLANAS alternatively optimizes the architecture on the local search stage and global search stage, and the weight entanglement strategy [45] is utilized to find optimal parameters at each stage. Firstly, the eight entanglement strategy [45] is directly employed to find optimal hyperparameters on the whole search space (As shown in Table I), which is denoted as the One stage searching. Then, the search space is divided into the global and local space by our GLANAS and we gradually perform global and local search for one time. This scheme is represented by the Two stage searching. Finally, we alternatively search the optimal hyperparameters on two stages until convergence, which is denoted as Alternative searching (GLANAS). The experimental results are shown in Table VI. The results of ablation experiments in Table VI show that the alternative searching on two stages achieves a significant accuracy improvement, which demonstrates that the space division and the alternating mechanism are helpful for NAS approaches to find optimal architecture parameters.

F. Feature Visualization Analysis

To investigate the performance of our approach, we visualize the heat maps of the last hidden layers in various approaches. As our GLVM approach includes the CNN and MHMamba branches, so we show the CNN, MHMamba, and dual-branch hybrid feature maps. Similarly, the CNN-based feature maps in ResNet50 [10], PVCNN [24], FVCNN [15], LWCNN [25], FVRASNet [17], Transformer-based feature maps in Vit [11], LE-MSVT [26], ALE-IVT [27], and Mamba-based feature maps in Vim [30], LocalVim [33] are extracted to estimate the performance. To facilitate comparison, we normalize the output maps in each channel to the same size as the input image and average the resulting maps of all channels to obtain the final heat map. The experimental results of various approaches are shown in Fig. 8. From the feature maps in Figs. 8(a)-(f), we can observe that CNN models focus on a few regions with high brightness in a palm image. By contrast, the single Mamba and Transformer models focus on more texture feature regions, which are distributed at different locations in Figs. 8(g)-(k). Also, we can see that the MHMamba branch (Fig. 8(g)) in our approach focuses on more object regions such as vein textures than other approaches, which demonstrates the excellent feature extraction performance of our MHMamba. Finally, for ALE-IVT (Fig. 8(m)) and our GLVM (Fig. 8(l)) which are both introduced local information, we can clearly observe that our approach extracts more precise global-local hybrid feature information, which conforms to the vein texture distribution, resulting in the powerful feature representation ability of our model.

VI. CONCLUSION

In this paper, we propose a vein recognition method to improve the accuracy and robustness of vein recognition. First, we investigate a global-local vision Mamba to take both advantages of convolution operations and state space model

for enhanced representation learning. Second, we propose a global-local alternating neural architecture search method to find optimal architecture hyperparameters. The experimental results on three public palm-vein databases show that our approach outperforms existing approaches and achieve a state of the art recognition performance. In the future, we explore the application of Mamba in other biometrics such as finger-vein recognition and face recognition.

REFERENCES

- [1] M.A. Turk and A.P. Pentland. Face recognition using eigenfaces. In *Proceedings. 1991 IEEE Computer Society Conference on Computer Vision and Pattern Recognition*, pages 586–591, 1991.
- [2] A. Jain, Lin Hong, and R. Bolle. On-line fingerprint verification. *IEEE Transactions on Pattern Analysis and Machine Intelligence*, 19(4):302–314, 1997.
- [3] J. Daugman. How iris recognition works. *IEEE Transactions on Circuits and Systems for Video Technology*, 14(1):21–30, 2004.
- [4] Huafeng Qin, Hongyu Zhu, Xin Jin, Qun Song, Mounim A. El-Yacoubi, and Xinbo Gao. Emmixformer: Mix transformer for eye movement recognition. *ArXiv*, abs/2401.04956, 2024.
- [5] Yantao Li, Song Ruan, Huafeng Qin, Shaojiang Deng, and Mounim A El-Yacoubi. Transformer based defense gan against palm-vein adversarial attacks. *IEEE Transactions on Information Forensics and Security*, 18:1509–1523, 2023.
- [6] Naoto Miura, Akio Nagasaka, and Takafumi Miyatake. Extraction of finger-vein patterns using maximum curvature points in image profiles. *Ice Transactions on Information & Systems*, 90(8):págs. 1185–1194, 2007.
- [7] T Liu, JB Xie, W Yan, PQ Li, and HZ Lu. An algorithm for finger-vein segmentation based on modified repeated line tracking. *The Imaging Science Journal*, 61(6):491–502, 2013.
- [8] Haiying Liu, Lingfei Song, Gongping Yang, Lu Yang, and Yilong Yin. Customized local line binary pattern method for finger vein recognition. In *Biometric Recognition: 12th Chinese Conference, CCBR 2017, Shenzhen, China, October 28-29, 2017, Proceedings 12*, pages 314–323. Springer, 2017.
- [9] Shuyi Li, Ruijun Ma, Lunke Fei, and Bob Zhang. Learning compact multirepresentation feature descriptor for finger-vein recognition. *IEEE Transactions on Information Forensics and Security*, 17:1946–1958, 2022.
- [10] Kaiming He, Xiangyu Zhang, Shaoqing Ren, and Jian Sun. Deep residual learning for image recognition. In *Proceedings of the IEEE Conference on Computer Vision and Pattern Recognition (CVPR)*, June 2016.
- [11] Alexey Dosovitskiy, Lucas Beyer, Alexander Kolesnikov, Dirk Weissenborn, Xiaohua Zhai, Thomas Unterthiner, Mostafa Dehghani, Matthias Minderer, Georg Heigold, Sylvain Gelly, et al. An image is worth 16x16 words: Transformers for image recognition at scale. *arXiv preprint arXiv:2010.11929*, 2020.
- [12] Huafeng Qin, Xin Jin, Yun Jiang, Mounim A. El-Yacoubi, and Xinbo Gao. Adversarial automixup. In *International Conference on Learning Representations*, 2024.
- [13] Huafeng Qin, Xin Jin, Hongyu Zhu, Hongchao Liao, Mounim A El-Yacoubi, and Xinbo Gao. Sumix: Mixup with semantic and uncertain information. *ECCV*, 2024.
- [14] Xin Jin, Hongyu Zhu, Mounim A. El-Yacoubi, Hongchao Liao, Huafeng Qin, and Yun Jiang. Starlknnet: Star mixup with large kernel networks for palm vein identification. *ArXiv*, abs/2405.12721, 2024.
- [15] Rig Das, Emanuela Piciucco, Emanuele Maiorana, and Patrizio Campisi. Convolutional neural network for finger-vein-based biometric identification. *IEEE Transactions on Information Forensics and Security*, 14(2):360–373, 2018.
- [16] Wenming Yang, Changqing Hui, Zhiqian Chen, Jing-Hao Xue, and Qingmin Liao. Fv-gan: Finger vein representation using generative adversarial networks. *IEEE Transactions on Information Forensics and Security*, 14(9):2512–2524, 2019.
- [17] Weili Yang, Wei Luo, Wenxiong Kang, Zhixing Huang, and Qiuxia Wu. Fvras-net: An embedded finger-vein recognition and ant spoofing system using a unified cnn. *IEEE Transactions on Instrumentation and Measurement*, 69(11):8690–8701, 2020.
- [18] Zaiyu Pan, Jun Wang, Guoqing Wang, and Jihong Zhu. Multi-scale deep representation aggregation for vein recognition. *IEEE Transactions on Information Forensics and Security*, 16:1–15, 2020.
- [19] S Veluchamy and LR Karlmarx. System for multimodal biometric recognition based on finger knuckle and finger vein using feature-level fusion and k-support vector machine classifier. *IET Biometrics*, 6(3):232–242, 2017.
- [20] Nurul Maisarah Kamaruddin and Bakhtiar Affendi Rosdi. A new filter generation method in pcanet for finger vein recognition. *IEEE Access*, 7:132966–132978, 2019.
- [21] Dawlat Mustafa Sulaiman, Adnan Mohsin Abdulazeez, Habibollah Haron, and Shereen S Sadiq. Unsupervised learning approach-based new optimization k-means clustering for finger vein image localization. In *2019 international conference on advanced science and engineering (ICOASE)*, pages 82–87. IEEE, 2019.
- [22] John Wright, Yi Ma, Julien Mairal, Guillermo Sapiro, Thomas S Huang, and Shuicheng Yan. Sparse representation for computer vision and pattern recognition. *Proceedings of the IEEE*, 98(6):1031–1044, 2010.
- [23] Lu Yang, Gongping Yang, Kuikui Wang, Fanchang Hao, and Yilong Yin. Finger vein recognition via sparse reconstruction error constrained low-rank representation. *IEEE Transactions on Information Forensics and Security*, 16:4869–4881, 2021.
- [24] Huafeng Qin, Mounim A. El-Yacoubi, Yantao Li, and Chongwen Liu. Multi-scale and multi-direction gan for cnn-based single palm-vein identification. *IEEE Transactions on Information Forensics and Security*, 16:2652–2666, 2021.
- [25] Jiaquan Shen, Ningzhong Liu, Chenglu Xu, Han Sun, Yushun Xiao, Deguang Li, and Yongxin Zhang. Finger

vein recognition algorithm based on lightweight deep convolutional neural network. *IEEE Transactions on Instrumentation and Measurement*, 71:1–13, 2021.

[26] Huafeng Qin, Changqing Gong, Yantao Li, Xinbo Gao, and Mounim A El-Yacoubi. Label enhancement-based multiscale transformer for palm-vein recognition. *IEEE Transactions on Instrumentation and Measurement*, 72:1–17, 2023.

[27] Huafeng Qin, Changqing Gong, Yantao Li, Mounim A El-Yacoubi, Xinbo Gao, and Jun Wang. Attention label learning to enhance interactive vein transformer for palm-vein recognition. *IEEE Transactions on Biometrics, Behavior, and Identity Science*, 2024.

[28] Mingsong Li, Yikun Liu, Tao Xiao, Yuwen Huang, and Gongping Yang. Local-global transformer enhanced unfolding network for pan-sharpening. *arXiv preprint arXiv:2304.14612*, 2023.

[29] Ashish Vaswani, Noam Shazeer, Niki Parmar, Jakob Uszkoreit, Llion Jones, Aidan N Gomez, Łukasz Kaiser, and Illia Polosukhin. Attention is all you need. *Advances in neural information processing systems*, 30, 2017.

[30] Lianghui Zhu, Bencheng Liao, Qian Zhang, Xinlong Wang, Wenyu Liu, and Xinggang Wang. Vision mamba: Efficient visual representation learning with bidirectional state space model. *ICML2024, arXiv preprint arXiv:2401.09417*, 2024.

[31] Albert Gu, Karan Goel, and Christopher Ré. Efficiently modeling long sequences with structured state spaces. In *The International Conference on Learning Representations (ICLR)*, 2022.

[32] Albert Gu and Tri Dao. Mamba: Linear-time sequence modeling with selective state spaces. *arXiv preprint arXiv:2312.00752*, 2023.

[33] Tao Huang, Xiaohuan Pei, Shan You, Fei Wang, Chen Qian, and Chang Xu. Localmamba: Visual state space model with windowed selective scan. *arXiv preprint arXiv:2403.09338*, 2024.

[34] Xiao Liu, Chenxu Zhang, and Lei Zhang. Vision mamba: A comprehensive survey and taxonomy. *arXiv preprint arXiv:2405.04404*, 2024.

[35] Ziyang Wang, Jian-Qing Zheng, Yichi Zhang, Ge Cui, and Lei Li. Mamba-unet: Unet-like pure visual mamba for medical image segmentation. *arXiv preprint arXiv:2402.05079*, 2024.

[36] Zhaohu Xing, Tian Ye, Yijun Yang, Guang Liu, and Lei Zhu. Segmamba: Long-range sequential modeling mamba for 3d medical image segmentation. *arXiv preprint arXiv:2401.13560*, 2024.

[37] Yao Teng, Yue Wu, Han Shi, Xuefei Ning, Guohao Dai, Yu Wang, Zhenguo Li, and Xihui Liu. Dim: Diffusion mamba for efficient high-resolution image synthesis. *arXiv preprint arXiv:2405.14224*, 2024.

[38] Zhiliang Peng, Zonghao Guo, Wei Huang, Yaowei Wang, Lingxi Xie, Jianbin Jiao, Qi Tian, and Qixiang Ye. Conformer: Local features coupling global representations for recognition and detection. *IEEE Transactions on Pattern Analysis and Machine Intelligence*, 2023.

[39] Barret Zoph and Quoc V Le. Neural architecture search with reinforcement learning. *arXiv preprint arXiv:1611.01578*, 2016.

[40] Esteban Real, Sherry Moore, Andrew Selle, Saurabh Saxena, Yutaka Leon Suematsu, Jie Tan, Quoc V Le, and Alexey Kurakin. Large-scale evolution of image classifiers. In *International conference on machine learning*, pages 2902–2911. PMLR, 2017.

[41] Gabriel Bender, Pieter-Jan Kindermans, Barret Zoph, Vijay Vasudevan, and Quoc Le. Understanding and simplifying one-shot architecture search. In *International Conference on Machine Learning*, pages 550–559. PMLR, 2018.

[42] Zichao Guo, Xiangyu Zhang, Haoyuan Mu, Wen Heng, Zechun Liu, Yichen Wei, and Jian Sun. Single path one-shot neural architecture search with uniform sampling. In *Computer Vision–ECCV 2020: 16th European Conference, Glasgow, UK, August 23–28, 2020, Proceedings, Part XVI 16*, pages 544–560. Springer, 2020.

[43] Wei Jia, Wei Xia, Yang Zhao, Hai Min, and Yan-Xiang Chen. 2d and 3d palmprint and palm vein recognition based on neural architecture search. *International Journal of Automation and Computing*, 18(3):377–409, 2021.

[44] Huafeng Qin, Chao Fan, Shaojiang Deng, Yantao Li, Mounim A El-Yacoubi, and Gang Zhou. Ag-nas: An attention gru-based neural architecture search for finger-vein recognition. *IEEE Transactions on Information Forensics and Security*, 2023.

[45] Minghao Chen, Houwen Peng, Jianlong Fu, and Haibin Ling. Autoformer: Searching transformers for visual recognition. In *Proceedings of the IEEE/CVF international conference on computer vision*, pages 12270–12280, 2021.

[46] Lu Yang, Gongping Yang, Yilong Yin, and Xiaoming Xi. Finger vein recognition with anatomy structure analysis. *IEEE Transactions on Circuits and Systems for Video Technology*, 28(8):1892–1905, 2017.

[47] Wenxiong Kang and Qiuxia Wu. Contactless palm vein recognition using a mutual foreground-based local binary pattern. *IEEE transactions on Information Forensics and Security*, 9(11):1974–1985, 2014.

[48] Wei-Yu Han and Jen-Chun Lee. Palm vein recognition using adaptive gabor filter. *Expert Systems with Applications*, 39(18):13225–13234, 2012.

[49] Yifan Wang, Huimin Lu, Xiwen Qin, and Jianwei Guo. Residual gabor convolutional network and fv-mix exponential level data augmentation strategy for finger vein recognition. *Expert Systems with Applications*, 223:119874, 2023.

[50] Yue Liu, Yunjie Tian, Yuzhong Zhao, Hongtian Yu, Lingxi Xie, Yaowei Wang, Qixiang Ye, and Yunfan Liu. Vmamba: Visual state space model. *arXiv preprint arXiv:2401.10166*, 2024.

[51] James Bergstra and Yoshua Bengio. Random search for hyper-parameter optimization. *Journal of machine learning research*, 13(2), 2012.

[52] Boyu Chen, Peixia Li, Chuming Li, Baopu Li, Lei Bai, Chen Lin, Ming Sun, Junjie Yan, and Wanli Ouyang. Glit: Neural architecture search for global and local

image transformer. In *Proceedings of the IEEE/CVF International Conference on Computer Vision*, pages 12–21, 2021.

- [53] Xiu Su, Shan You, Jiyang Xie, Mingkai Zheng, Fei Wang, Chen Qian, Changshui Zhang, Xiaogang Wang, and Chang Xu. Vitas: Vision transformer architecture search. In *European Conference on Computer Vision*, pages 139–157. Springer, 2022.
- [54] Albert Gu, Isys Johnson, Karan Goel, Khaled Saab, Tri Dao, Atri Rudra, and Christopher Ré. Combining recurrent, convolutional, and continuous-time models with linear state space layers. *Advances in Neural Information Processing Systems (NPIS)*, 34:572–585, 2021.
- [55] Jianyuan Guo, Kai Han, Han Wu, Yehui Tang, Xinghao Chen, Yunhe Wang, and Chang Xu. Cmt: Convolutional neural networks meet vision transformers. In *Proceedings of the IEEE/CVF conference on computer vision and pattern recognition*, pages 12175–12185, 2022.
- [56] Biao Zhang and Rico Sennrich. Root mean square layer normalization. *Advances in Neural Information Processing Systems*, 32, 2019.
- [57] Dan Hendrycks and Kevin Gimpel. Gaussian error linear units (gelus). *arXiv preprint arXiv:1606.08415*, 2016.
- [58] Lin Zhang, Zaixi Cheng, Ying Shen, and Dongqing Wang. Palmprint and palmvein recognition based on dcnn and a new large-scale contactless palmvein dataset. *Symmetry*, 10(4):78, 2018.
- [59] Pedro Tome and Sébastien Marcel. On the vulnerability of palm vein recognition to spoofing attacks. In *2015 International Conference on Biometrics (ICB)*, pages 319–325. IEEE, 2015.
- [60] David Zhang, Zhenhua Guo, Guangming Lu, Lei Zhang, and Wangmeng Zuo. An online system of multispectral palmprint verification. *IEEE transactions on instrumentation and measurement*, 59(2):480–490, 2009.
- [61] Huafeng Qin, Mounim A El Yacoubi, Jihai Lin, and Bo Liu. An iterative deep neural network for hand-vein verification. *IEEE Access*, 7:34823–34837, 2019.
- [62] Hongyi Zhang, Moustapha Cisse, Yann N Dauphin, and David Lopez-Paz. mixup: Beyond empirical risk minimization. In *International Conference on Learning Representation (ICLR)*, 2018.
- [63] Ilya Loshchilov, Frank Hutter, et al. Fixing weight decay regularization in adam. *arXiv preprint arXiv:1711.05101*, 5, 2017.
- [64] Chengyue Gong and Dilin Wang. Nasvit: Neural architecture search for efficient vision transformers with gradient conflict-aware supernet training. *ICLR Proceedings 2022*, 2022.
- [65] Ramprasaath R Selvaraju, Michael Cogswell, Abhishek Das, Ramakrishna Vedantam, Devi Parikh, and Dhruv Batra. Grad-cam: visual explanations from deep networks via gradient-based localization. *International journal of computer vision*, 128:336–359, 2020.